

Turning Trash into Treasure: MXene with Intrinsic LiF Solid Electrolyte Interfaces Performs Better and Better during Battery Cycling

Hao Xu, Wen Zhu, Fengzhan Sun, Hu Qi, Jianxin Zou,* Richard Laine,* and Wenjiang Ding

Commercialization of lithium ion batteries has accelerated dramatically over the last few decades. Single-layered Ti_3C_2 ($s\text{-Ti}_3\text{C}_2$) is effectively prepared by etching Ti_3AlC_2 via simple treatment with HCl and LiF, producing inevitably sediments always discarded after etching. This study explores the effect of LiF doping of multilayered Ti_3C_2 to form $m\text{-Ti}_3\text{C}_2/\text{LiF}$ consisting essentially of the sediments. Simple half-cells assembled with $m\text{-Ti}_3\text{C}_2/\text{LiF}$ sediments suggest that LiF suppresses electrode volume expansion and surface cracking during cycling promoting Li^+ intercalation/deintercalation. The data also suggest that LiF promotes formation of stable artificial solid electrolyte interfaces to prevent electrolyte and electrode degradation. The capacity of $m\text{-Ti}_3\text{C}_2/\text{LiF}$ sediments derived cells maintains 136 mAh g^{-1} after 1500 cycles at 300 mA g^{-1} while $s\text{-Ti}_3\text{C}_2$ from supernatants physically mixed with 20 wt% LiF shows a capacity of 335 mAh g^{-1} (100th cycle) at 100 mA g^{-1} with an initial coulombic efficiency of 83%. Half-cell anodes made of Ti_3C_2 etched by HF, commercial TiO_2 , and Sn powder mixed physically with 20 wt% LiF exhibit improved performance with cycling. These results indicate that the always discarded sediments can be directly used in LIBs and simple doping with LiF obviously improves the electrochemical performance of materials.

1. Introduction

Rechargeable lithium ion batteries (LIBs) are sought as a means to meet society's ever-increasing energy demands. Motivation comes from the fact that LIBs offer potential environment as eco-friendly, sustainable and highly effective energy sources.^[1–4] Thus, great efforts are being made to enhance energy densities and power output of LIBs.^[5] In particular, significant focus is on greatly improving current anode materials. Mainstream graphite anodes LIBs (theoretical capacity of 372 mAh g^{-1}) offer insufficient rate capabilities and suffer from uneven lithium plating.^[6,7]

The discovery, by Novoselov et al., of a method of preparing 2D materials (graphene) has attracted worldwide attention.^[8] Graphene-like materials can offer excellent optical, electric, and magnetic properties, which make them attractive for applications in a wide variety of energy storage and conversion devices.^[9–12] These materials include hexagonal boron nitride (h-BN),^[13] transition metal disulfides,^[12] metal oxides, and bilayer hydroxides.^[14]

Recent reports on 2D transition metal carbides and carbonitrides, MXenes,^[15,16] have prompted efforts to consider them for battery applications.^[17] MXene materials are prepared mainly by selectively etching the A layers from the 3D $\text{M}_{n+1}\text{AlX}_n$ ($n = 1, 2, 3$) parent phase, where “M” represents a transition metal, “A” is a group III or IV-A element, and X is carbon and/or nitrogen. The exfoliation process was initially conducted using hydrofluoric acid (HF), producing multilayered M_{n+1}X_n ($m\text{-M}_{n+1}\text{X}_n$) with surface functional OH, F, and O groups. A more benign approach uses concentrated hydrochloric acid (HCl) and lithium fluoride (LiF) mixtures as the etching medium resulting in colloidal supernatant. The colloidal supernatant is composed predominantly of single-layered M_{n+1}X_n ($s\text{-M}_{n+1}\text{X}_n$) coincident with Li^+ intercalation,^[18] while the sediments contain primarily $m\text{-M}_{n+1}\text{X}_n$ and intercalated LiF.


MXenes have now been explored extensively for electrochemical energy storage,^[19–21] in electronic devices,^[22,23] as hydrogen storage materials,^[24] and as separation membranes.^[25] Ti_3C_2 , a typical MXene, has drawn considerable attention for use

H. Xu, W. Zhu, F. Z. Sun, H. Qi, Prof. J. X. Zou, Prof. W. J. Ding
National Engineering Research Center of Light Alloy Net Forming
School of Materials Science and Engineering
Shanghai Jiao Tong University
Shanghai 200240, P. R. China
E-mail: zoujx@sjtu.edu.cn

H. Xu, W. Zhu, F. Z. Sun, H. Qi, Prof. J. X. Zou, Prof. W. J. Ding
State Key Laboratory of Metal Matrix Composites
School of Materials Science and Engineering
Shanghai Jiao Tong University
Shanghai 200240, P. R. China

H. Xu, W. Zhu, F. Z. Sun, H. Qi, Prof. J. X. Zou, Prof. W. J. Ding
Center of Hydrogen Science
Shanghai Jiao Tong University
Shanghai 200240, P. R. China

Prof. R. M. Laine
Department of Materials Science and Engineering
University of Michigan
Ann Arbor, MI 48109-2136, USA
E-mail: talsdad@umich.edu

 The ORCID identification number(s) for the author(s) of this article can be found under <https://doi.org/10.1002/admt.202000882>.

DOI: 10.1002/admt.202000882

in LIBs. Tang et al. described DFT calculations indicating that pure Ti_3C_2 should offer a theoretical specific capacity of 320 mAh g^{-1} as anodes for LIBs with the capacity decreasing to 130 and 67 mAh g^{-1} when Ti_3C_2 is superficially functionalized with F ($\text{Ti}_3\text{C}_2\text{F}_2$) and OH [$\text{Ti}_3\text{C}_2(\text{OH})_2$] respectively.^[26] These surface functionalized Ti_3C_2 materials were reported to exhibit a capacity of 124 mAh g^{-1} at 320 mA g^{-1} after 100 cycles due to Li^+ intercalation via a conversion reaction.^[27]

Numerous Ti_3C_2 composites have been synthesized targeting improved electrochemical performance,^[28] including $\text{Ti}_3\text{C}_2@\text{rGO}$,^[20] $\text{Ti}_3\text{C}_2@\text{CNTs}$,^[29] $\text{Ti}_3\text{C}_2@\text{TiO}_2$,^[30] $\text{Ti}_3\text{C}_2@\text{SnO}_2$,^[31] and $\text{Ti}_3\text{C}_2@\text{Si}$.^[32] Ti_3C_2 offers hydrophilic surfaces, electronic conductivity, low operating voltages 0.2–0.6 V versus Li^+/Li , low diffusion barriers (due to surface functional groups), and stable layered structures (due to Ti–C bonds) with exceptional mechanical properties, which are important to Li^+ intercalation.^[31] Therefore, Ti_3C_2 seems to be an ideal matrix template for LIB anode composites.^[33]

Single-layered Ti_3C_2 ($s\text{-Ti}_3\text{C}_2$) is easily obtained by first etching Al from Ti_3AlC_2 and then delaminating the multilayered Ti_3C_2 ($m\text{-Ti}_3\text{C}_2$) using HCl and LiF. This stepwise procedure generates mixtures of undelaminated $m\text{-Ti}_3\text{C}_2$ containing up to 90% of the original LiF used.^[34] The $m\text{-Ti}_3\text{C}_2/\text{LiF}$ sediments are normally ignored or disposed, which greatly increases synthesis cost and hinders applications in LIBs. Note that LiF is the main inorganic component in solid electrolyte interfaces (SEIs) that form in commercial LIBs, offering a wide electrochemical stability window with negligible solubility in most electrolytes solvents as well as a relatively low energy barrier for Li^+ diffusion.^[35,36]

Peng et al. developed a transplantable LiF-rich layer to improve the cycling stability of Li metal anodes where Li^+ can diffuse through this artificial layer and deposit on the Cu or Li substrate surfaces.^[37] Sun et al. developed an extremely simple cell formation process to simultaneously form LiF-rich protective-films on the surfaces of both CNT-cathodes and Li metal anodes.^[38] Shen et al. successfully prepared graphite fluoride (GF)–LiF–Li composites that bond with metallic lithium and are stable on contact with a carbonate electrolyte.^[39] Zhu et al. showed that the lithium storage performance of MoS_2 could be improved by facilitating the generation of a robust LiF-rich

SEI by adding fluoroethylene carbonate to prevent continuous electrolyte decomposition.^[40] On this basis, the resulting sediments produced here were chosen as a starting point to develop anodes for LIBs with well-defined architecture.

The objective of the current work is to show how LiF influences the electrochemical performance of $m\text{-Ti}_3\text{C}_2/\text{LiF}$ sediment [$m\text{-Ti}_3\text{C}_2/\text{LiF}(\text{S}_1)$] anodes for LIBs. The source of these materials from sediments is simply the “debris” recovered from the etching process without additional additives and displays some abnormal (advantageous) electrochemical properties. The rationally fabricated cells exhibit gradually increasing capacities after initial capacity fading, in which they maintain 198 mAh g^{-1} (600th cycle) at 30 mA g^{-1} and 136 mAh g^{-1} (1500th cycle) at 300 mA g^{-1} while $s\text{-Ti}_3\text{C}_2$ from supernatants physically mixed with 20 wt% LiF shows a reversible capacity of 335 mAh g^{-1} (100th cycle) at 100 mA g^{-1} , which is comparable to previous reports of MXene anodes for LIBs (Table S1, Supporting Information). Additionally, intrinsic LiF serves as an artificial SEI and Li^+ diffusion shuttle, appearing to play a significant role in restraining the expansion and cracking of electrodes as well as improving the electrochemical performance.

2. Results and Discussion

Figure 1 provides a general overview of the processing steps (detailed in the Experimental Section, Supporting Information) that lead to formation of $m\text{-Ti}_3\text{C}_2/\text{LiF}(\text{S}_1)$ consisting of sediments and $s\text{-Ti}_3\text{C}_2$ consisting of supernatants via HCl + LiF etching of Ti_3AlC_2 . The $m\text{-Ti}_3\text{C}_2/\text{LiF}(\text{S}_1)$ is easily separated from $s\text{-Ti}_3\text{C}_2$ supernatant by high speed centrifugation.

Figure S1 (Supporting Information) presents XRD analyses of some samples. The precursor XRD pattern, Ti_3AlC_2 powder, presents characteristic peaks labeled as \blacklozenge . The peaks marked as \star of Ti_3C_2 etched by HF suggest some loss of crystallinity with structural distortions compared with Ti_3AlC_2 . Also, the characteristic (002) and (004) planes broaden and shift to lower angles 2θ arising from increases in d- and layer- spacing. Notably, the intensity of the peak at $\approx 39^\circ 2\theta$, corresponding to the (104) plane of the Ti_3AlC_2 , weakens significantly, suggesting successful removal of Al layers from Ti_3AlC_2 and formation of Ti_3C_2 .^[41]

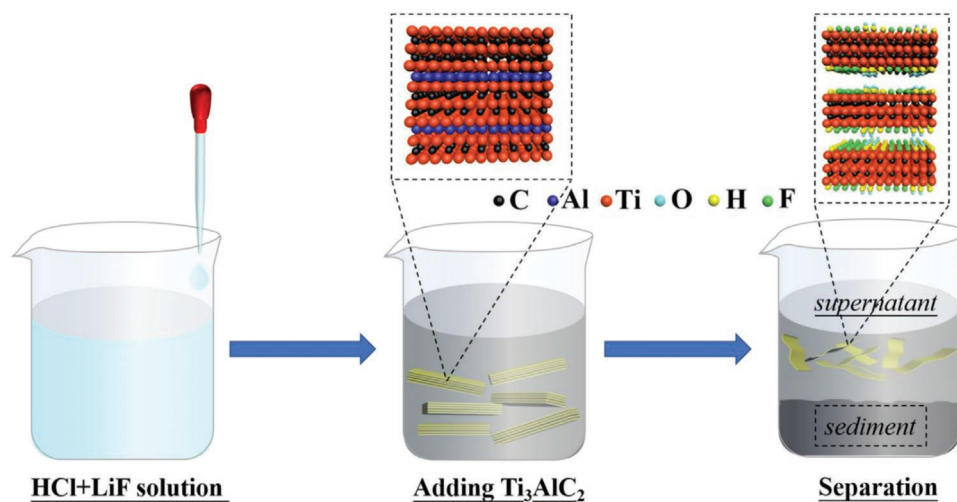


Figure 1. General methods used to prepare $m\text{-Ti}_3\text{C}_2/\text{LiF}$ sediments.

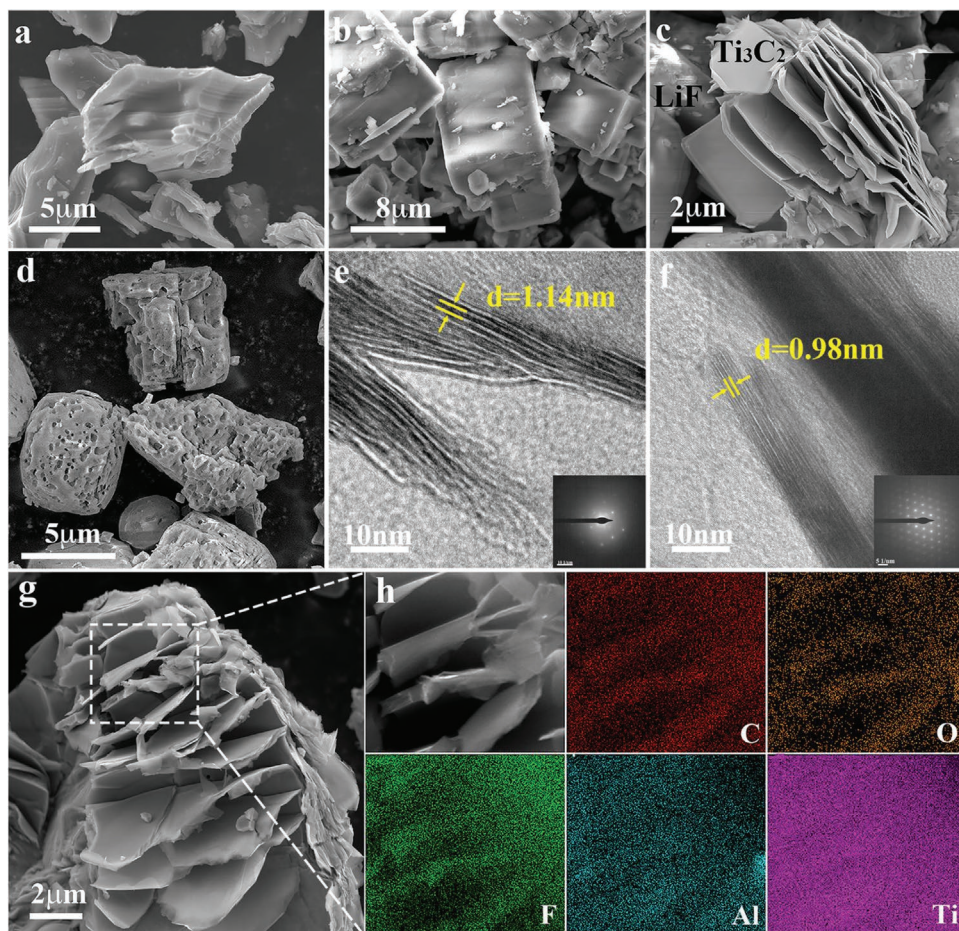


Figure 2. SEM of a) Ti_3AlC_2 , b) LiF before etching, c) $m\text{-Ti}_3\text{C}_2$ etched by HCl + LiF, d) LiF after etching. HRTEM image (inset is SAED image) of e) $m\text{-Ti}_3\text{C}_2$ etched by HCl + LiF and f) Ti_3C_2 etched by HF. g,h) SEM and EDX of $m\text{-Ti}_3\text{C}_2$ etched by HCl + LiF.

In addition, $m\text{-Ti}_3\text{C}_2/\text{LiF}(\text{S}_1)$ diffraction peaks match closely those of Ti_3C_2 including (002), (103), (105), and (112) planes (marked as ★). The LiF peak pattern, especially for (111), (200), and (220) planes, is also clearly present (marked as ▲). These peaks are unshifted versus crystalline LiF, indicating its presence after etching. Moreover, (002) peak of Ti_3AlC_2 appears in this pattern, indicating that not all the Ti_3AlC_2 -phase converts to $m\text{-Ti}_3\text{C}_2$, while a small amount of Ti_3AlC_2 exists in the sediments further evidenced by EDX and XPS. Besides, the presence of $a \approx 39^\circ 2\theta$ peak (Figure S2, Supporting Information) shows that etching using $\text{MgF}_2 + \text{HCl}$ offers end-products of $m\text{-Ti}_3\text{C}_2/\text{MgF}_2$ sediment [$m\text{-Ti}_3\text{C}_2/\text{MgF}_2(\text{S}_2)$], demonstrating relatively low etching efficiency.

The morphologies of Ti_3AlC_2 , LiF, Ti_3C_2 , $m\text{-Ti}_3\text{C}_2/\text{LiF}(\text{S}_1)$, and $m\text{-Ti}_3\text{C}_2/\text{MgF}_2(\text{S}_2)$ were characterized by SEM and TEM. As shown in Figure 2a, Ti_3AlC_2 presents irregular 3D blocks. Figure 2b exhibits typical LiF cube morphology. Figure S3 and Table S2 (Supporting Information) show typical book-like morphology and elemental mapping results of Ti_3C_2 , which are typical etching results by HF. Figure 2c shows that the remaining LiF particles are mixed with the $m\text{-Ti}_3\text{C}_2$ particles after HCl + LiF etching. To verify the success of the etching procedure when HCl and LiF were used, EDX analyses of $m\text{-Ti}_3\text{C}_2$ selected from local areas in Figure 2g of $m\text{-Ti}_3\text{C}_2/\text{LiF}(\text{S}_1)$ are presented in Figure 2h and Table S3 (Supporting

Information). These results demonstrate that C, O, F, Al, and Ti are homogeneously distributed. Mapping for Al shows a minimal amount of 1.58 wt%, mainly ascribed to the unreacted Ti_3AlC_2 .

During the reaction process, excess dissolved LiF apparently penetrates the layered structure and crystallizes within the resulting samples and remains even after etchant treated samples are rinsed more than a dozen times. Coincident with etching and deposition of LiF nanoparticles the smooth surface gradually erodes (Figure 2d). By contrast, Figure S4 (Supporting Information) shows that the formed $m\text{-Ti}_3\text{C}_2/\text{MgF}_2(\text{S}_2)$ retain their book-like morphology with rough surfaces. Elemental mapping results (Table S4, Supporting Information) indicating that Al is not fully etched by HCl + MgF_2 .

TEM images of Ti_3C_2 etched by HF and HCl + LiF reveal separated layers. The results are in good agreement with the above SEM results. The formed edges are similar to the graphitic layers reported previously.^[42] The cross-sectional HRTEM images in Figure 2e,f show that the layer spacing of Ti_3C_2 etched by HCl + LiF is 1.14 nm, a little larger than that etched by HF alone (0.98 nm). The inset in Figure 2e does not show similar hexagonal packing behavior, see inset in Figure 2f, most easily interpreted as being caused by the presence of crystalline LiF and Ti_3AlC_2 . The distinct interlayer pores of etched Ti_3C_2 provide sites for Li^+ interaction.^[43]

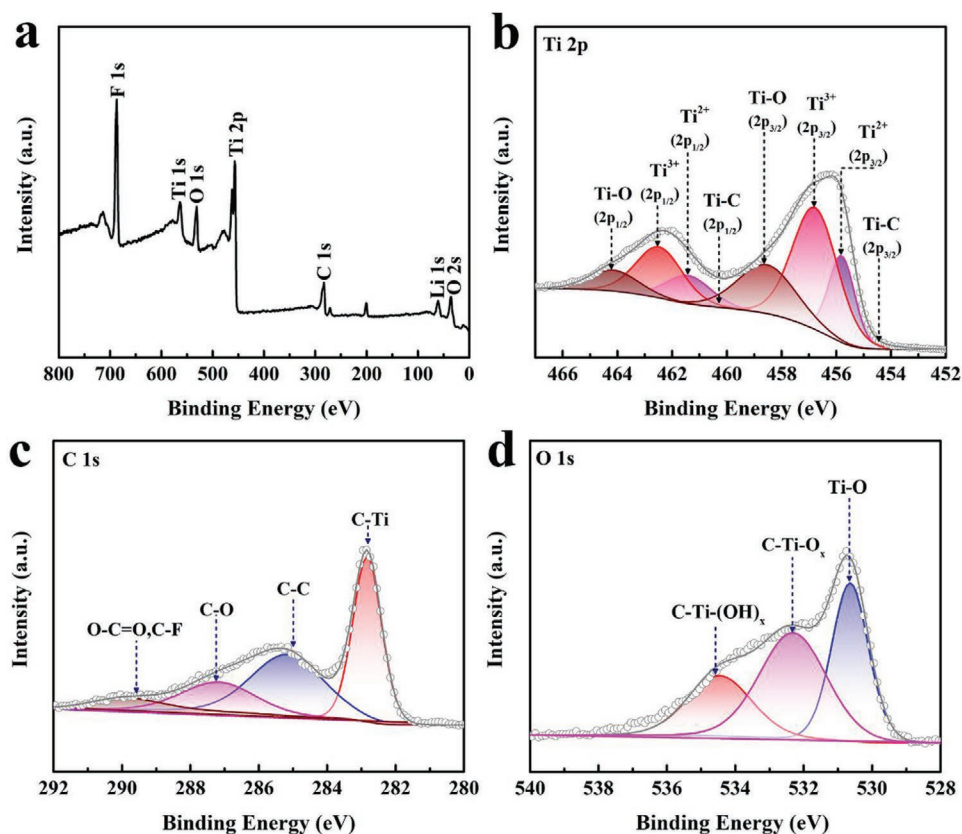
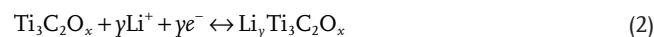


Figure 3. XPS spectra of the $m\text{-Ti}_3\text{C}_2/\text{LiF}(\text{S}_1)$. a) Survey spectrum, b) Ti 2p, c) C 1s, and d) O 1s.

XPS was used to confirm the chemical composition, bonding, and oxidation states in the $m\text{-Ti}_3\text{C}_2/\text{LiF}(\text{S}_1)$. The low-resolution survey spectrum (Figure 3a) shows that typical elemental signatures for $m\text{-Ti}_3\text{C}_2/\text{LiF}(\text{S}_1)$ primarily consist of Ti, O, C, F, and Li. The LiF content is calculated to be 36.8 wt% (Table S5, Supporting Information). As presented in Figure 3b, XPS peak fitting indicates that the Ti 2p spectrum of $m\text{-Ti}_3\text{C}_2/\text{LiF}(\text{S}_1)$ can be resolved into four sets of $2p_{3/2}\text{-}2p_{1/2}$ spin-orbit doublets with a fixed area ratio of 2:1 and doublet separation of 5.7 eV. The Ti $2p_{3/2}$ peaks centered at 454.5, 455.8, 456.8, and 458.5 eV correspond to Ti-C, Ti^{2+} , Ti^{3+} , and Ti-O, respectively.^[44-46] A small amount of TiO_2 forms from reaction between Ti_3C_2 and the OH caused by heat generated during HCl + LiF treatment as reported previously.^[47] The C 1s binding energies presented in Figure 3c at 289.7, 287.1, 285.1, and 282.8 eV correspond to O-C=O and C-F, C-O, C-C, and Ti-C.^[48] In addition, the O 1s spectrum for $m\text{-Ti}_3\text{C}_2/\text{LiF}(\text{S}_1)$ presents peaks at 530.6, 532.4, and 534.6 eV (Figure 3d), matching Ti-O in TiO_2 , C-Ti-O_x and C-Ti-(OH)_x respectively.^[31] Compared with those for Ti_3C_2 etched by HF alone (Figure S5, Supporting Information), there is a slight increase in the intensity of the Ti^{3+} , Ti^{2+} , C-C, C-Ti peaks accompanied by a decrease in the intensity of Ti-O, C-F, C-O, and C-Ti-(OH)_x peaks (Tables S6 and S7, Supporting Information). The results indicate somewhat greater oxidation of Ti and formation of TiO_2 during the HCl + LiF etching process.

LIB anodes prepared from the $m\text{-Ti}_3\text{C}_2/\text{LiF}(\text{S}_1)$ were assembled (see the Experimental Section). CV curves in voltage range of 0.01–3.00 V at a sweep rate of 0.1 mV s^{-1} are shown

in Figure 4a for the first three cycles. During the initial lithiation, irreversible peaks are observed at 0.76, 1.43, and 1.64 V, close to those of Ti_3C_2 (0.8 and 1.56 V) presented in Figure S6 (Supporting Information). However, they are absent in subsequent cycles, ascribed to formation of an SEI and trapping of Li^+ between Ti_3C_2 flakes in the electrode.^[49] In the first delithiation step, two broad anodic peaks are seen at 1.56 and 2.33 V, respectively, which diminish slightly in subsequent cycles, corresponding to extraction of Li^+ from the $m\text{-Ti}_3\text{C}_2/\text{LiF}(\text{S}_1)$ electrode, suggesting that charge storage is due to the intercalation of Li^+ rather than a conversion reaction.^[27] The cathodic and anodic peaks near 0.01 V correspond to lithiation/delithiation of the Super-P carbon.^[49] In all subsequent cycles, broad and weak reversible peaks are observed at 0.89 and 1.00 V compared with those of Li^+/Li related to intercalation and deintercalation in the $m\text{-Ti}_3\text{C}_2/\text{LiF}(\text{S}_1)$, respectively (Equation (1)). Figure S6 (Supporting Information) shows anodic (1.00 V) and cathodic (0.91 V) peaks indicating similar Li^+ intercalation and deintercalation. Also, weak reversible peaks appear at 1.60 and 1.89 V versus Li^+/Li during lithiation/delithiation process, respectively, tentatively ascribed to a possible reaction similar to that reported between TiO_2 and lithiated titania (Equation (2))^[50]



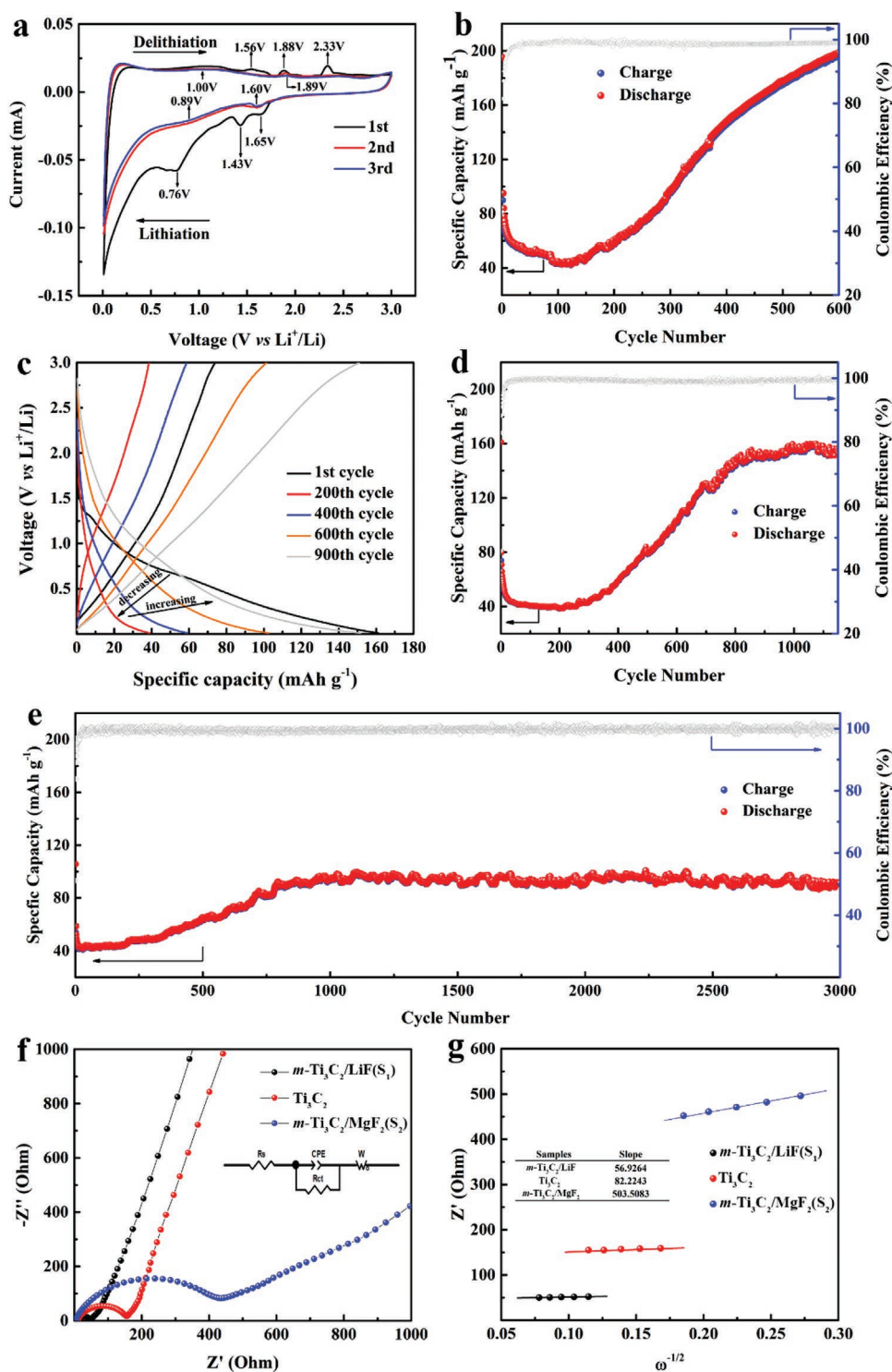


Figure 4. Electrochemical evaluation of *m*-Ti₃C₂/LiF(S₁). a) CV curves at 0.1 mV s⁻¹ for the first three cycles, Long term cycling performance at b) 30, d) 150, e) 600 mA g⁻¹, c) and charge/discharge profiles during the 1st, 200th, 400th, 600th, and 900th cycles at 150 mA g⁻¹. f) Electrochemical impedance spectra (inset is equivalent circuit diagram) and g) linear fitting Z' versus ω^{-1/2} in the low-frequency region of Ti₃C₂, *m*-Ti₃C₂/LiF(S₁) and *m*-Ti₃C₂/MgF₂(S₂).

As presented in Figure 4b, at 30 mA g⁻¹, the first charge and discharge capacities of *m*-Ti₃C₂/LiF(S₁) for LIBs are 90 and 195 mAh g⁻¹, respectively. The large initial capacity loss likely arises for two reasons: 1) consumption of the electrolyte to form

SEI and 2) irreversible reduction at the surface electrochemical active area. The 100th charge and discharge capacities of Ti₃C₂/LiF hybrids are 45 and 45 mAh g⁻¹ with a Coulombic efficiency of 100%. After long term cycling, the charge/discharge

capacities of $m\text{-Ti}_3\text{C}_2/\text{LiF}(\text{S}_1)$ increase dramatically to 197 and 198 mAh g⁻¹, a nearly 340% capacity increase compared with the initial low capacity. Ti_3C_2 from $m\text{-Ti}_3\text{C}_2/\text{LiF}(\text{S}_1)$ contributes to the electrode capacities via intercalation/deintercalation reactions by tolerating the expansion/contraction of the interlayer distance during cyclic Li⁺ intercalation/deintercalation.^[51–53] The decreasing lithium ion diffusion barriers and increasing Li⁺ storage capacities are significantly assigned to the expansion of Ti_3C_2 interlayer spacing. Moreover, LiF used as etchant during preparation of $m\text{-Ti}_3\text{C}_2/\text{LiF}$ sediments shows a reversible capacity of 20 mAh g⁻¹ at 100 mA g⁻¹ presented in Figure S7 (Supporting Information), thus contributing a little to the capacity of $m\text{-Ti}_3\text{C}_2/\text{LiF}(\text{S}_1)$.

The cycling results at 150 and 600 mA g⁻¹ are presented in the Figure 4d,e. At 150 mA g⁻¹, $m\text{-Ti}_3\text{C}_2/\text{LiF}(\text{S}_1)$ shows charge capacities of 74, 39, 59, 102, and 151 mAh g⁻¹ and discharge capacities of 161, 39, 59, 102, and 151 mAh g⁻¹, respectively, at 1st, 200th, 400th, 600th, and 900th cycles. Also, the charge/discharge profiles during the 1st, 200th, 400th, 600th, and 900th cycles shown in Figure 4c are in good agreement with the results shown in Figure 4d. When the current density increases to 600 mA g⁻¹, the capacities should decrease. In detail, the first charge and discharge capacities of $m\text{-Ti}_3\text{C}_2/\text{LiF}(\text{S}_1)$ are 54 and 106 mAh g⁻¹ respectively. With the capacities decreasing initially and then increasing, the 1000th charge and discharge capacities are 94 and 94 mAh g⁻¹, respectively, with a columbic efficiency of 100%. By the 3000th charge and discharge, capacities both retain 91 mAh g⁻¹.

The cycling comparison (Figure S8, Supporting Information) shows that the electrochemical performance of $m\text{-Ti}_3\text{C}_2/\text{LiF}(\text{S}_1)$ is much better than those of $m\text{-Ti}_3\text{C}_2/\text{MgF}_2(\text{S}_2)$ and Ti_3C_2 . In detail, the capacities of $m\text{-Ti}_3\text{C}_2/\text{LiF}(\text{S}_1)$ and $m\text{-Ti}_3\text{C}_2/\text{MgF}_2(\text{S}_2)$ exhibit a common feature: decreasing initially, then gradually increasing and finally stabilizing with increasing cycle numbers, while the capacities of Ti_3C_2 first decrease sharply, then decrease gradually. The charge capacities of $m\text{-Ti}_3\text{C}_2/\text{LiF}(\text{S}_1)$, $m\text{-Ti}_3\text{C}_2/\text{MgF}_2(\text{S}_2)$, and Ti_3C_2 after 1500 cycles are 136, 52, and 50 mAh g⁻¹, respectively, at 300 mA g⁻¹. The obvious distinction shows that LiF plays a significant role in increasing the capacity.

To determine the conductivity and ion transport properties, Figure 4f compares the Nyquist plots of Ti_3C_2 , $m\text{-Ti}_3\text{C}_2/\text{LiF}(\text{S}_1)$, and $m\text{-Ti}_3\text{C}_2/\text{MgF}_2(\text{S}_2)$. Each plot consists of two parts: a semicircle at high frequency and a straight line at low frequency, which correspond to charge transfer resistance (R_{ct}) and Warburg impedance (W) associated with Li⁺ diffusion in the bulk electrode. R_{ct} is a combination of the electrolyte-accessible area and electrical conductivity of the electrode. A larger electroactive surface area leads to lower R_{ct} . Apparently, the fitting results (Figure 4g; Table S8, Supporting Information) indicate that the semicircle diameter of $\text{Ti}_3\text{C}_2/\text{LiF}(\text{S}_1)$ matches an R_{ct} value of 33 Ω, lower than that of Ti_3C_2 (127 Ω) and $m\text{-Ti}_3\text{C}_2/\text{MgF}_2(\text{S}_2)$ (427 Ω), indicating a lower charge transfer resistance. Nevertheless, the electronic resistance (R_s) of $m\text{-Ti}_3\text{C}_2/\text{LiF}(\text{S}_1)$ (6.4 Ω) stays in the middle of those of Ti_3C_2 (9.5 Ω) and $m\text{-Ti}_3\text{C}_2/\text{MgF}_2(\text{S}_2)$ (3.5 Ω).

The diffusion coefficients of Li⁺ are calculated as follows

$$D_{\text{Li}^+} = \frac{R^2 T^2}{2A^2 n^4 F^4 c^2 \sigma^2} \quad (3)$$

Here R is the gas constant ($R = 8.314 \text{ J mol}^{-1} \text{ K}^{-1}$), T is the absolute temperature ($T = 298 \text{ K}$), A is the polar area ($A = 1.13 \text{ cm}^2$), n is the number of electron transfers ($n = 1$) and F is the Faraday constant ($F = 96485 \text{ C mol}^{-1}$). c is the concentration of lithium ion electrolyte ($c = 1 \text{ mol L}^{-1}$). The calculated results are presented in Table S8 (Supporting Information). The D_{Li^+} of $m\text{-Ti}_3\text{C}_2/\text{LiF}(\text{S}_1)$ ($4.9 \times 10^{-16} \text{ cm}^2 \text{ s}^{-1}$) is higher than that for Ti_3C_2 ($3.4 \times 10^{-16} \text{ cm}^2 \text{ s}^{-1}$). These values are an order of magnitude greater than that of $m\text{-Ti}_3\text{C}_2/\text{MgF}_2(\text{S}_2)$ ($5.5 \times 10^{-17} \text{ cm}^2 \text{ s}^{-1}$). The low diffusion rate for $m\text{-Ti}_3\text{C}_2/\text{MgF}_2(\text{S}_2)$ may arise from incomplete etching of the parent phase and the sluggish transport of Mg^{2+} . These results support the idea that $m\text{-Ti}_3\text{C}_2/\text{LiF}(\text{S}_1)$ show better electrochemical performance due to introduction of extra LiF. Thus, LiF can effectively diffuse into the interlayer channels of Ti_3C_2 , thereby achieving faster ion transfer than the sample etched by that without LiF.

CV was run for $m\text{-Ti}_3\text{C}_2/\text{LiF}(\text{S}_1)$ electrode for LIBs at different sweep rates (0.1–0.8 mV s⁻¹) after 1000 cycles (Figure 5a) at 300 mA g⁻¹ to explore the charge transfer mechanism of the materials. The logarithm of the sweep rate (ν) and peak current (i) is linear through the following formula

$$i = a\nu^b \Leftrightarrow \log i = b \log \nu + \log a \quad (4)$$

The magnitude of the slope b reflects control of the electrochemical reaction. When $b = 0.5$, the peak current exhibits a linear relationship with the square root of the sweep rate ($\nu^{1/2}$), indicating that the reaction process is a typical diffusion-controlled battery storage process. When $b = 1$, the peak current is proportional to the sweep rate, revealing capacitive-controlled energy storage behavior.^[54,55] Figure 5b shows that the b values of the anodic (peak A) and cathodic (peak B) peaks are 0.90 and 0.89, suggesting that a capacitive-controlled energy storage mechanism cannot be ignored in the $m\text{-Ti}_3\text{C}_2/\text{LiF}(\text{S}_1)$ electrodes.

On the basis of the relationship between current value ($i(V)$) and fixed voltage (V), the total capacitance contribution at a certain sweep rate can be quantified by the following equation through the separation of the specific capacitive ($k_1\nu$) and diffusion control ($k_2\nu^{1/2}$) contributions

$$i(V) = k_1\nu + k_2\nu^{1/2} \Leftrightarrow i(V) / \nu^{1/2} = k_1\nu^{1/2} + k_2 \quad (5)$$

The quantitative calculation results presented in Figure 5c and Figure S9 (Supporting Information) show that the capacitive contributions at 0.1, 0.2, 0.4, 0.6, and 0.8 mV s⁻¹ are 55.9%, 60.4%, 68.2%, 73.7%, and 78.0%, respectively. Moreover, the proportion of capacitive-controlled capacity increases with increasing sweep rates (Figure 5d), indicating that the capacitive behavior is more useful for Li⁺ intercalation/deintercalation at higher sweep rates, owing to the rapid charge/discharge characteristic of the energy storage mechanism. The $m\text{-Ti}_3\text{C}_2/\text{LiF}(\text{S}_1)$ successfully combine the dynamic equilibrium of fast capacitive-controlled pseudo-capacitance and high diffusion-controlled energy storage, providing considerable electrochemical performance for LIBs.

The ex situ SEM images of fresh electrodes, electrodes after 200, 600, and 1200 cycles for Ti_3C_2 and $m\text{-Ti}_3\text{C}_2/\text{LiF}(\text{S}_1)$ at 300 mA g⁻¹ are given in Figure 6 respectively to verify the volume effect and structural stability of materials for LIBs. As displayed in Figure 6a–d, the fresh $m\text{-Ti}_3\text{C}_2/\text{LiF}(\text{S}_1)$ electrode

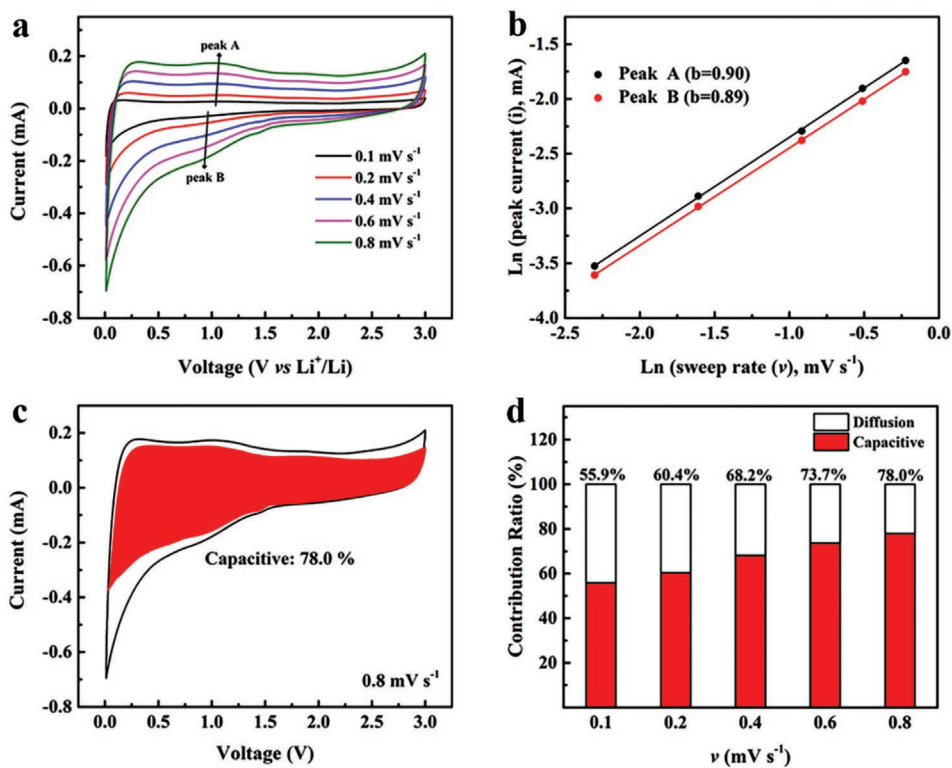


Figure 5. Kinetic analyses of electrochemical behavior for LIBs. a) CV curves of $m\text{-Ti}_3\text{C}_2/\text{LiF}(\text{S}_1)$ electrode at various sweep rates from 0.1 to 0.8 mV s^{-1} after 1000 cycles. b) Relationship between peak currents and sweep rates (plotted with natural logarithm axis). c) CV curve with corresponding capacitive contribution at 0.8 mV s^{-1} . d) Capacitive contribution ratios at different sweep rates.

before cycling exhibits a longitudinal thickness of 17.1 μm , where the operating electrodes after 200, 600, and 1200 cycles

increases slightly to 18.4, 19.4, and 20.1 μm respectively with a final expansion of 17.5%.

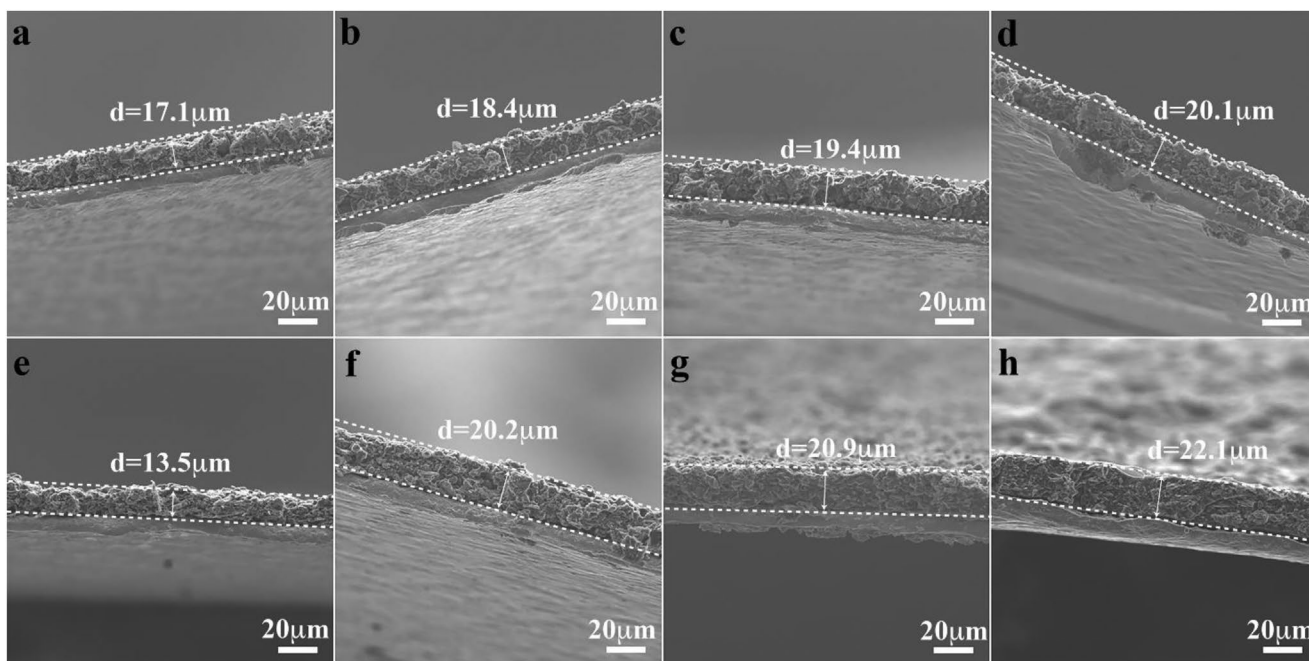


Figure 6. Cross-sectional SEM images of the electrodes for LIBs in fully charged state. a) Fresh electrode, electrodes after b) 200, c) 600, and d) 1200 cycles at 300 mA g^{-1} for $m\text{-Ti}_3\text{C}_2/\text{LiF}(\text{S}_1)$. e) Fresh electrode, electrodes after f) 200, g) 600, and h) 1200 cycles at 300 mA g^{-1} for Ti_3C_2 .

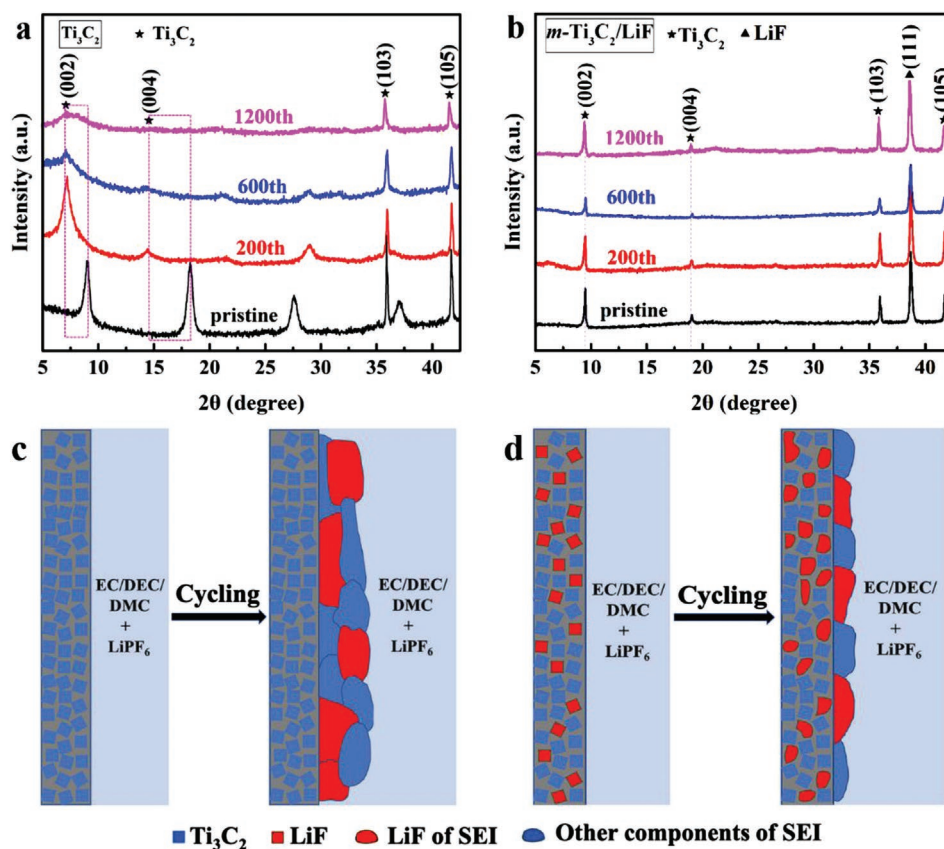


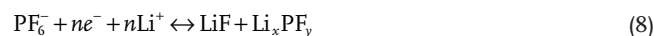
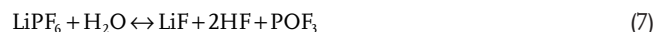
Figure 7. Ex situ XRD of the electrodes in fully charged state. a) Fresh electrode, electrodes after 200, 600, and 1200 cycles at 300 mA g⁻¹ for Ti₃C₂. b) Fresh electrode, electrodes after 200, 600, and 1200 cycles at 300 mA g⁻¹ for *m*-Ti₃C₂/LiF(S₁). Conceptual schemes of SEI formation for electrolytes containing EC/DEC/DMC and LiPF₆ on the electrodes of c) Ti₃C₂ and d) *m*-Ti₃C₂/LiF(S₁).

For comparison, the Ti₃C₂ electrodes show one major increase in thickness, before cycling (13.5 μm, Figure 6e), after 200 cycles (20.2 μm, Figure 6f), after 600 cycles (20.9 μm, Figure 6g) and after 1200 cycles (22.1 μm, Figure 6h) with a expansion ratio of 63.7%, thereby indicating the limitation in the volume change of the electrodes during cycling when LiF penetrates. Furthermore, Figure S10 (Supporting Information) indicates that Ti₃C₂ electrode surface exhibits cracks without LiF after 600 cycles at 300 mA g⁻¹, and even worse after 1200 cycles. These cracks lead to electrode polarization and effectiveness of the active material, thereby causing capacity fading and reducing battery cycling life. Interestingly, this phenomenon is not observed on the surfaces of *m*-Ti₃C₂/LiF(S₁) electrodes during cycling.

Ex situ XRD of fresh electrode, electrodes after 200, 600, and 1200 cycles for Ti₃C₂ in fully charged state are shown in Figure 7a. The characteristic planes, (002) and (004), shift dramatically to lower angle, as Ti₃C₂ structure changes considerably during cycling. Nevertheless, when LiF present, the characteristic (002) and (004) planes (Figure 7b) exhibit no obvious shift with the increasing cycle numbers, demonstrating a negligible structural change with long term cycling. Overall, it implies that LiF prevents the electrode from expanding and cracking, enhancing Ti₃C₂ performance in LIBs.

It is reasonable to propose a simple mechanism to explain the role of LiF during LIB cycling. Previous investigations suggest that electrode SEI in commercial LIBs is unstable and evolves

over calendar life cycling,^[35,56] resulting in the changes in the SEI composition. The changes include typically an increase in the concentration of inorganic species such as LiF caused by primary side reactions shown in Equations (6)–(9).^[35–36,57,58] First, the decomposition of the electrolyte accompanied by LiF generation occurs with difficulty owing to Le Chatelier's principle, hindering the SEI formation on Ti₃C₂/LiF(S₁) electrode surfaces. Then the LiF in Ti₃C₂/LiF(S₁) performs as an artificial SEI on the electrode (Figure 7d), creating shuttles for Li⁺ diffusion. Nevertheless, a simple Ti₃C₂ electrode without LiF will see formation of an SEI induced by electrolyte decomposition during cycling (Figure 7c), causing the electrode to thicken and crack. LiF not only provides protective SEIs for the electrodes but also serves as a Li⁺ shuttle, enhancing the electrochemical performance during battery cycling to great extent



Except for the “always discarded” sediments, Figure 8a,b indicates that single-layered MXene (*s*-Ti₃C₂) collected from the

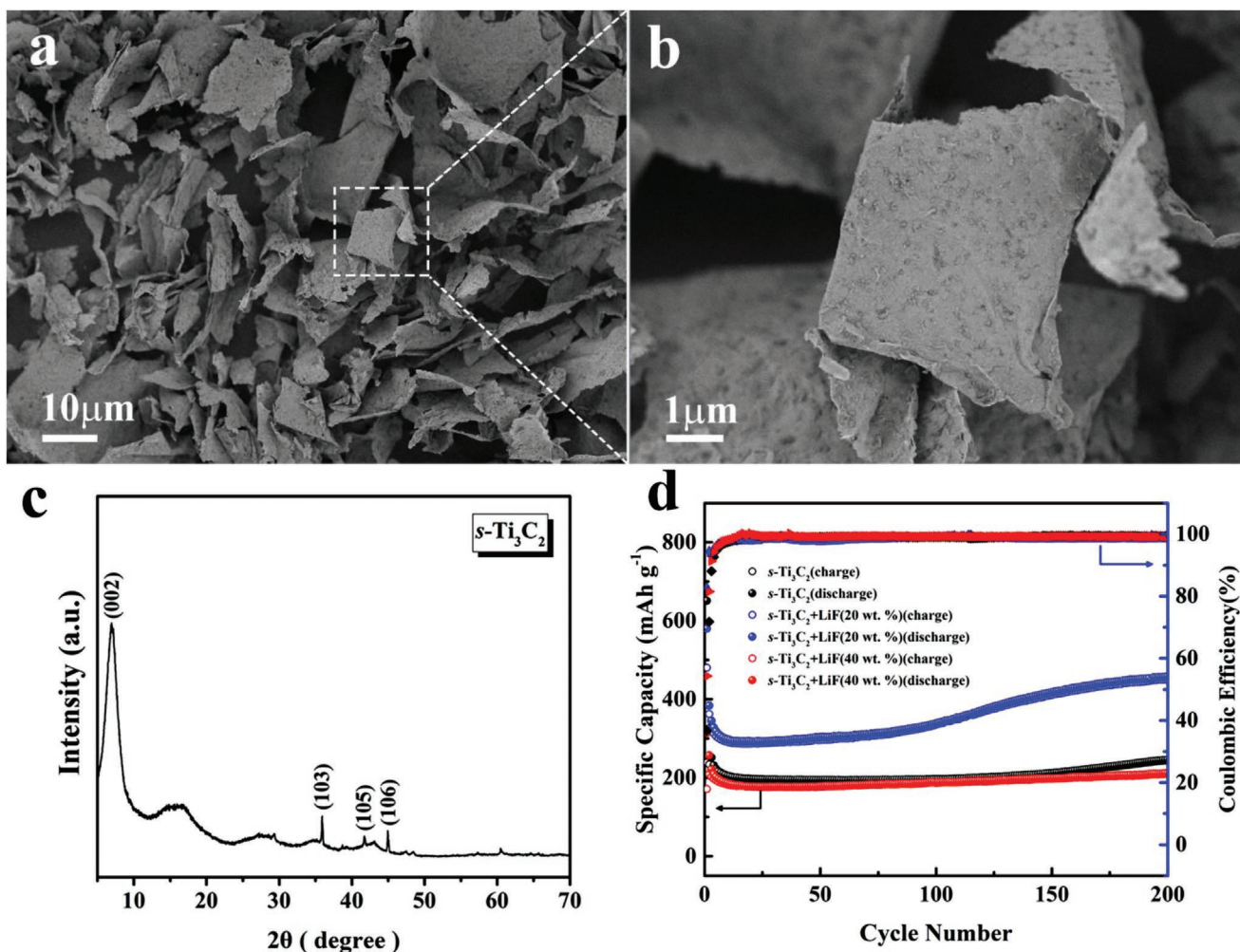


Figure 8. a,b) SEM of $s\text{-Ti}_3\text{C}_2$ from the supernatant at different scales. c) XRD of $s\text{-Ti}_3\text{C}_2$. d) Cycling performance of $s\text{-Ti}_3\text{C}_2$, $s\text{-Ti}_3\text{C}_2 + \text{LiF}$ (20 wt%), and $s\text{-Ti}_3\text{C}_2 + \text{LiF}$ (40 wt%) at 100 mA g^{-1} for LIBs.

supernatants shows a 2D morphology. The XRD (Figure 8c) shows that (002) peak shifts to lower angle compared with Ti_3AlC_2 (Figure 1a) and (104) peak disappears, verifying the successful preparation of $s\text{-Ti}_3\text{C}_2$. When applied in LIBs, $s\text{-Ti}_3\text{C}_2$ electrode shows a reversible capacity of 194 mAh g^{-1} at 100 mA g^{-1} after 100 cycles. When $s\text{-Ti}_3\text{C}_2$ physically mixed with LiF powder at different weigh ratio, $s\text{-Ti}_3\text{C}_2 + \text{LiF}$ (20 wt%) and $s\text{-Ti}_3\text{C}_2 + \text{LiF}$ (40 wt%) electrodes show reversible capacities of 335 and 186 mAh g^{-1} respectively (Figure 8d). Besides, $s\text{-Ti}_3\text{C}_2 + \text{LiF}$ (20 wt%) electrode shows the highest coulombic efficiency of 83% than $s\text{-Ti}_3\text{C}_2$ (37%) and $s\text{-Ti}_3\text{C}_2 + \text{LiF}$ (40 wt%) (54%) for first cycle. First, LiF in $s\text{-Ti}_3\text{C}_2 + \text{LiF}$ mixtures performs as an artificial SEI on the electrode, improving the initial coulombic efficiency and alleviating the capacity decaying during battery cycling. Also, LiF should create shuttles for Li^+ diffusion, enhancing the electrochemical performance. On the other hand, excessive LiF will reduce capacity of the electrodes owing to the low capacity of LiF. Besides, the conductivity of the electrodes will be decreased to some extent when LiF added.^[59] Thus, an appropriate amount of LiF is significant for the $s\text{-Ti}_3\text{C}_2$ electrodes.

As a control set of studies, LiF (20 wt%) was mixed separately with different materials including Ti_3C_2 , anatase TiO_2 , and commercial tin (Sn) powder, and then assembled as electrodes for LIBs. Figure S11 (Supporting Information) shows that the capacities of $\text{Ti}_3\text{C}_2 + \text{LiF}$ and Ti_3C_2 are 168 and 50 mAh g^{-1} at 300 mA g^{-1} after 1500 cycles. Previous researches reported that there was a great volume change in the process of charge/discharge of tin anode ($>260\%$) for LIBs,^[60,61] leading to a sharp decline in capacity. However, for Sn powder mixed with 20 wt% LiF powder, Figure S12 of the Supporting Information presents that reversible capacities of Sn + LiF are 158, 120, and 40 mAh g^{-1} , respectively, at 50, 100, and 500 mA g^{-1} , which are greater than those of sole Sn (62, 41, and 24 mAh g^{-1} , respectively). These results suggest that LiF can enhance the capacity of such kinds of materials typically found to undergo significant expansion during cycling in LIB formats. The volume change for anatase TiO_2 used in LIBs during cycling was less than 5%.^[62–64] Figure S13 (Supporting Information) indicates that the reversible capacities of TiO_2 are 44, 35, and 25 mAh g^{-1} , respectively, at 50, 100, and 500 mA g^{-1} , slightly less than those of $\text{TiO}_2 + \text{LiF}$ (57, 40, and 37 mAh g^{-1} , respectively). These

results further indicate that enhanced electrochemical performance can be mainly ascribed to the LiF penetration, especially for these materials undergoing great volume change during cycling.

3. Conclusion

Etching Ti_3AlC_2 using HCl and LiF results in supernatants containing $s\text{-Ti}_3\text{C}_2$ as end-products and $m\text{-Ti}_3\text{C}_2/\text{LiF}$ sediments [$m\text{-Ti}_3\text{C}_2/\text{LiF}(\text{S}_1)$] always discarded as “debris.” Ti_3C_2 from $m\text{-Ti}_3\text{C}_2/\text{LiF}(\text{S}_1)$ sample presents book-like microstructures with some LiF impregnated into Ti_3C_2 . LiF not only suppresses expansion of $m\text{-Ti}_3\text{C}_2/\text{LiF}(\text{S}_1)$ electrodes for LIBs during cycling but also increases capacities with increasing cycle numbers. The results confirm that LiF enhances the electrochemical properties, structural stability, and ion migration rates. On the one hand, Ti_3C_2 acts as a skeleton to accelerate electron and ion migration. On the other hand, LiF serves as a Li^+ transfer shuttle for insertion and extraction, forming a stable artificial SEI to prevent electrolyte and electrode degradation, thereby integrating the merits of both components. Also, $m\text{-Ti}_3\text{C}_2/\text{LiF}(\text{S}_1)$ possess superior high-rate and long-term cycling performance due to pseudocapacitance. Besides, $s\text{-Ti}_3\text{C}_2 + \text{LiF}$ (20 wt%) shows considerable initial coulombic efficiency and reversible capacity. Thus, the introduction of LiF can be a very simple and efficient route paving the way to enhance the electrochemical performance for LIBs, as well as reducing cost of synthesis for MXene by making full use of the sediments.

Supporting Information

Supporting Information is available from the Wiley Online Library or from the author.

Acknowledgements

This work was supported by the National Natural Science Foundation of China (Grant No. 51771112), the Science and Technology Commission of Shanghai Municipality (CN) under Grant No. 19511108100, and Shanghai Education Commission “Shuguang” scholar project (CN, 16SG08).

Conflict of Interest

The authors declare no conflict of interest.

Keywords

capacity increasing, LiF, lithium ion batteries, MXene, Ti_3C_2

Received: September 4, 2020
Revised: November 22, 2020
Published online: February 8, 2021

- [1] J. Jiang, Q. Fan, S. Chou, Z. Guo, K. Konstantinov, H. Liu, J. Wang, *Small* **2019**, 1903934.
- [2] J. B. Goodenough, K. S. Park, *J. Am. Chem. Soc.* **2013**, 135, 1167.
- [3] S. Choi, G. Wang, *Adv. Mater. Technol.* **2018**, 3, 1700376.
- [4] K. Zhao, Y. Yang, X. Liu, Z. L. Wang, *Adv. Energy Mater.* **2017**, 7, 1700103.
- [5] Y. Dong, H. Shi, Z. S. Wu, *Adv. Funct. Mater.* **2020**, 30, 2000706.
- [6] Y. Cheng, Z. Yi, C. Wang, Y. Wu, L. Wang, *Chem. Eng. J.* **2017**, 330, 1035.
- [7] B. Scrosati, J. Hassoun, Y.-K. Sun, *Energy Environ. Sci.* **2011**, 4, 3287.
- [8] K. S. Novoselov, A. K. Geim, S. V. Morozov, D. Jiang, Y. Zhang, S. V. Dubonos, I. V. Grigorieva, A. A. Firsov, *Science* **2004**, 306, 666.
- [9] M. Xu, T. Liang, M. Shi, H. Chen, *Chem. Rev.* **2013**, 113, 3766.
- [10] P. K. Sahoo, S. Memaran, Y. Xin, L. Balicas, H. R. Gutierrez, *Nature* **2018**, 553, 63.
- [11] B. J. Kooi, B. Noheda, *Science* **2016**, 353, 221.
- [12] L. M. Xie, *Nanoscale* **2015**, 7, 18392.
- [13] D. Golberg, Y. Bando, Y. Huang, T. Terao, M. Mitome, C. C. Tang, C. Y. Zhi, *ACS Nano* **2010**, 4, 2979.
- [14] M. Chhowalla, H. S. Shin, G. Eda, L. J. Li, K. P. Loh, H. Zhang, *Nat. Chem.* **2013**, 5, 263.
- [15] M. Naguib, M. Kurtoglu, V. Presser, J. Lu, J. Niu, M. Heon, L. Hultman, Y. Gogotsi, M. W. Barsoum, *Adv. Mater.* **2011**, 23, 4248.
- [16] M. Naguib, O. Mashtalir, J. Carle, V. Presser, J. Lu, L. Hultman, Y. Gogotsi, W. Michel, *ACS Nano* **2012**, 6, 1322.
- [17] C. Zhang, Y. Ma, X. Zhang, S. Abdolhosseinzadeh, H. Sheng, W. Lan, A. Pakdel, J. Heier, F. Nüesch, *Energy Environ. Mater.* **2020**, 3, 29.
- [18] M. Ghidui, M. R. Lukatskaya, M. Q. Zhao, Y. Gogotsi, M. W. Barsoum, *Nature* **2014**, 516, 78.
- [19] W. Bao, L. Liu, C. Wang, S. Choi, D. Wang, G. Wang, *Adv. Energy Mater.* **2018**, 8, 1702485.
- [20] Z. Ma, X. Zhou, W. Deng, D. Lei, Z. Liu, *ACS Appl. Mater. Interfaces* **2018**, 10, 3634.
- [21] M. Q. Zhao, X. Xie, C. E. Ren, T. Makaryan, B. Anasori, G. Wang, Y. Gogotsi, *Adv. Mater.* **2017**, 29, 1702410.
- [22] E. Balci, U. O. Akkus, S. Berber, *ACS Appl. Mater. Interfaces* **2019**, 11, 3609.
- [23] A. Iqbal, P. Sambyal, C. M. Koo, *Adv. Funct. Mater.* **2020**, 30, 2000883.
- [24] Q. Hu, D. Sun, Q. Wu, H. Wang, L. Wang, B. Liu, A. Zhou, J. He, *J. Phys. Chem. A* **2013**, 117, 14253.
- [25] Z. Xu, Y. Sun, Y. Zhuang, W. Jing, H. Ye, Z. Cui, *J. Membr. Sci.* **2018**, 564, 35.
- [26] Q. Tang, Z. Zhou, P. Shen, *J. Am. Chem. Soc.* **2012**, 134, 16909.
- [27] D. Sun, M. Wang, Z. Li, G. Fan, L.-Z. Fan, A. Zhou, *Electrochem. Commun.* **2014**, 47, 80.
- [28] C. Zhang, L. Cui, S. Abdolhosseinzadeh, J. Heier, *InfoMat* **2020**, 2, 613.
- [29] C. E. Ren, M.-Q. Zhao, T. Makaryan, J. Halim, M. Boota, S. Kota, B. Anasori, M. W. Barsoum, Y. Gogotsi, *ChemElectroChem* **2016**, 3, 689.
- [30] C. Yang, Y. Liu, X. Sun, Y. Zhang, L. Hou, Q. Zhang, C. Yuan, *Electrochim. Acta* **2018**, 271, 165.
- [31] D.-c. Zuo, S.-c. Song, C.-s. An, L.-b. Tang, Z.-j. He, J.-c. Zheng, *Nano Energy* **2019**, 62, 401.
- [32] X. Hui, R. Zhao, P. Zhang, C. Li, C. Wang, L. Yin, *Adv. Energy Mater.* **2019**, 9, 1901065.
- [33] X. Wu, Z. Wang, M. Yu, L. Xiu, J. Qiu, *Adv. Mater.* **2017**, 29, 1607017.
- [34] S. Abdolhosseinzadeh, R. Schneider, A. Verma, J. Heier, F. Nüesch, C. J. Zhang, *Adv. Mater.* **2020**, 32, 2000716.
- [35] G. E. Peled, G. Ardel, *J. Electrochem. Soc.* **1997**, 144, L208.
- [36] S. K. Heiskanen, J. Kim, B. L. Lucht, *Joule* **2019**, 3, 2322.
- [37] Z. Peng, N. Zhao, Z. Zhang, H. Wan, H. Lin, M. Liu, C. Shen, H. He, X. Guo, J.-G. Zhang, D. Wang, *Nano Energy* **2017**, 39, 662.

- [38] Z. Sun, H.-R. Wang, J. Wang, T. Zhang, *Energy Storage Mater.* **2019**, 23, 670.
- [39] X. Shen, Y. Li, T. Qian, J. Liu, J. Zhou, C. Yan, J. B. Goodenough, *Nat. Commun.* **2019**, 10, 900.
- [40] Z. Zhu, Y. Tang, Z. Lv, J. Wei, Y. Zhang, R. Wang, W. Zhang, H. Xia, M. Ge, X. Chen, *Angew. Chem., Int. Ed.* **2018**, 57, 3656.
- [41] M. Alhabeab, K. Maleski, B. Anasori, P. Lelyukh, L. Clark, S. Sin, Y. Gogotsi, *Chem. Mater.* **2017**, 29, 7633.
- [42] J. Pang, R. G. Mendes, A. Bachmatiuk, L. Zhao, H. Q. Ta, T. Gemming, H. Liu, Z. Liu, M. H. Rummeli, *Chem. Soc. Rev.* **2019**, 48, 72.
- [43] X. Liang, A. Garsuch, L. F. Nazar, *Angew. Chem., Int. Ed.* **2015**, 54, 3907.
- [44] Y. Dall'Agnese, M. R. Lukatskaya, K. M. Cook, P.-L. Taberna, Y. Gogotsi, P. Simon, *Electrochem. Commun.* **2014**, 48, 118.
- [45] C. Peng, X. Yang, Y. Li, H. Yu, H. Wang, F. Peng, *ACS Appl. Mater. Interfaces* **2016**, 8, 6051.
- [46] Y. T. Liu, P. Zhang, N. Sun, B. Anasori, Q. Z. Zhu, H. Liu, Y. Gogotsi, B. Xu, *Adv. Mater.* **2018**, 30, 1707334.
- [47] R. B. Rakhi, B. Ahmed, M. N. Hedhili, D. H. Anjum, H. N. Alshareef, *Chem. Mater.* **2015**, 27, 5314.
- [48] X. Zhang, Y. Liu, S. Dong, Z. Ye, Y. Guo, *Ceram. Int.* **2017**, 43, 11065.
- [49] N. Sun, B.-y. Yang, J.-c. Zheng, Z.-j. He, H. Tong, L.-b. Tang, C.-s. An, B. Xiao, *Ceram. Int.* **2018**, 44, 16214.
- [50] Z. Yang, D. Choi, S. Kerisit, K. M. Rosso, D. Wang, J. Zhang, G. Graff, J. Liu, *J. Power Sources* **2009**, 192, 588.
- [51] C. Li, Z. Xue, J. Qin, M. Sawangphruk, P. Yu, X. Zhang, R. Liu, *J. Alloys Compd.* **2020**, 842, 155812.
- [52] Y. Z. Fang, R. Hu, K. Zhu, K. Ye, J. Yan, G. Wang, D. Cao, *Adv. Funct. Mater.* **2020**, 30, 2005663.
- [53] C. Zhang, M. Liang, S.-H. Park, Z. Lin, A. Seral-Ascaso, L. Wang, A. Pakdel, C. Ó. Coileáin, J. Boland, O. Ronan, N. McEvoy, B. Lu, Y. Wang, Y. Xia, J. N. Coleman, V. Nicolosi, *Energy Environ. Sci.* **2020**, 13, 2124.
- [54] T. Yuan, Y. Jiang, W. Sun, B. Xiang, Y. Li, M. Yan, B. Xu, S. Dou, *Adv. Funct. Mater.* **2016**, 26, 2198.
- [55] L. B. Tang, B. Zhang, C. S. An, H. Li, B. Xiao, J. H. Li, Z. J. He, J. C. Zheng, *Inorg. Chem.* **2019**, 58, 8169.
- [56] M. Broussely, P. Biensan, F. Bonhomme, P. Blanchard, S. Herreyre, K. Nechev, R. J. Staniewicz, *J. Power Sources* **2005**, 146, 90.
- [57] I. W. D. Aurbach, A. Zaban, O. Chusid, *Electrochim. Acta* **1994**, 39, 51.
- [58] T. Li, X.-Q. Zhang, P. Shi, Q. Zhang, *Joule* **2019**, 3, 2647.
- [59] W. Huang, H. Wang, D. T. Boyle, Y. Li, Y. Cui, *ACS Energy Lett.* **2020**, 5, 1128.
- [60] P. Sun, J. Davis, L. Cao, Z. Jiang, J. B. Cook, H. Ning, J. Liu, S. Kim, F. Fan, R. G. Nuzzo, P. V. Braun, *Energy Storage Mater.* **2019**, 17, 151.
- [61] H. Li, Z. Wang, L. Chen, X. Huang, *Adv. Mater.* **2009**, 21, 4593.
- [62] J. S. Chen, Z. Wang, X. C. Dong, P. Chen, X. W. Lou, *Nanoscale* **2011**, 3, 2158.
- [63] Y. Li, J. Shen, J. Li, S. Liu, D. Yu, R. Xu, W.-F. Fu, X.-J. Lv, *J. Mater. Chem. A* **2017**, 5, 7055.
- [64] J.-Y. Shin, D. Samulielis, J. Maier, *Adv. Funct. Mater.* **2011**, 21, 3464.